

## Coupled hydroelastic vibrations of a liquid on flexible space structures under zero-gravity - Part I. Mechanical model

Masakatsu Chiba<sup>\*1</sup>, Shinya Chiba<sup>2</sup> and Kousuke Takemura<sup>3</sup>

<sup>1</sup>Department of Aerospace Engineering, Graduate School of Engineering, Osaka Prefecture University, 1-1 Gakuen-cho, Naka-ku, Sakai, Osaka 599-8531, Japan

<sup>2</sup>Keihin corporation, 2021-8, Hosyakuji, Takanezawa-machi, Tochigi 329-1233, Japan

<sup>3</sup>NTN corporation, 1578, Higashi-Kaizuka, Iwata, Shizuoka 438-8510, Japan

(Received December 10, 2013, Revised February 10, 2014, Accepted February 14, 2014)

**Abstract.** The coupled free vibration of flexible structures and on-board liquid in zero gravity space was analyzed, considering the spacecraft main body as a rigid mass, the flexible appendages as two elastic beams, and the on-board liquid as a “spring-mass” system. Using the *Lagrangians* of a rigid mass (spacecraft main body), “spring-mass” (liquid), and two beams (flexible appendages), as well as assuming symmetric motion of the system, we obtained the frequency equations of the coupled system by applying *Rayleigh-Ritz* method. Solving these frequency equations, which are governed by three system parameters, as an eigenvalue problem, we obtained the coupled natural frequencies and vibration modes. We define the parameter for evaluating the magnitudes of coupled motions of the added mass (liquid) and beam (appendages). It was found that when varying one system parameter, the frequency curves veer, vibration modes exchange, and the significant coupling occurs not in the region closest to the two frequency curves but in the two regions separate from that region.

**Keywords:** hydroelastic vibration; space structure; coupled system; sloshing

---

### 1. Introduction

Space structures such as satellites vibrate easily at low frequencies because these structures have low structural rigidity resulting from the need for being lightweight. Owing to attitude control or orbit modification through thruster injection, flexible appendages such as antennas and solar arrays, as well as the liquid fuel or wastewater at the space station, may vibrate and develop strong coupled vibrations having a complex effect on the dynamic behavior of the main body. This would be a major concern for high-attitude-accuracy satellites such as those used for particularly precise astronomical photography. Therefore, it is essential to clarify in advance the dynamic interaction behavior of a flexible space structure with onboard liquid for improving the stability and reliability of space structures.

Many researchers have theoretically studied the sloshing of liquids in containers in low-gravity environments. For example, Abramson (1996) organized the studies undertaken until 1966. Bauer *et al.* (1990a and b) have conducted free vibration analysis of a liquid in a rectangular or

---

\*Corresponding author, Professor, E-mail: [chiba@aero.osakafu-u.ac.jp](mailto:chiba@aero.osakafu-u.ac.jp)

cylindrical vessel considering the liquid meniscus due to surface tension; furthermore, they carried out response analysis for a container under horizontal excitation. Agrawal (1993) analyzed the dynamic behavior of liquid in a rotating space vehicle using the boundary-layer model. Komatsu (1999) theoretically investigated the sloshing frequency in a space vehicle tank using a mechanical model and furthered the study using potential flow models to obtain the natural frequencies via a semi-empirical formula. Chiba *et al.* (2002) investigated the coupled natural vibration of an elastic membrane bottom and a liquid in a cylindrical container with a rigid wall, considering two types of free surface boundary conditions at the wall, i.e., the slipping condition and the anchored condition. Utsumi (2004) proposed mechanical models for sloshing in a tear-shaped axisymmetric tank, which is often used in spin-stabilized satellites, and showed the effects of the liquid-filling level and the Bond number on the parameters governing the sloshing characteristics. He *et al.* (2007) carried out a nonlinear analysis of liquid sloshing in a cylindrical container considering the static meniscus shape in low-gravity environments using the energy method under pitching excitation around the cylinder's center of gravity. Berglund *et al.* (2007) controlled the sloshing of liquid propellant in a Delta IV rocket following the pulse suppression approach and summarized the analytical results related to liquid behavior in a potential flow model.

However, there are only a few experimental studies that focus on resolving the sloshing that occurs in low-gravity environments. In 2005, the Netherlands Agency for Aerospace, NIVR, launched a 130-kg miniature satellite called “Sloshsat Flevo” with an 87-L tank including 33.5 L of water for investigating the effect of sloshing behaviors on the satellite's motion, see Vreeburg (2008). Experiments were carried on the satellite to observe the behavior of the internal liquid due to thruster injection.

Then, with regard to the effects of sloshing motion on spacecraft motion, McIntyre and McIntyre (1982) revealed the relationship between the balance and stability of flat rotating spacecraft with on-board liquid fuel. Santini and Barboni (1978, 1983) analyzed the influence of motion around the center of gravity on sloshing in on-orbit space structures through force balance and argued about its stability. Lü *et al.* (2005) analyzed the vibration due to liquid motion in a rectangular tank with flexible appendages subjected to pitching excitation using the energy method under conditions of microgravity and gravity; they clarified that coupling between the liquid and

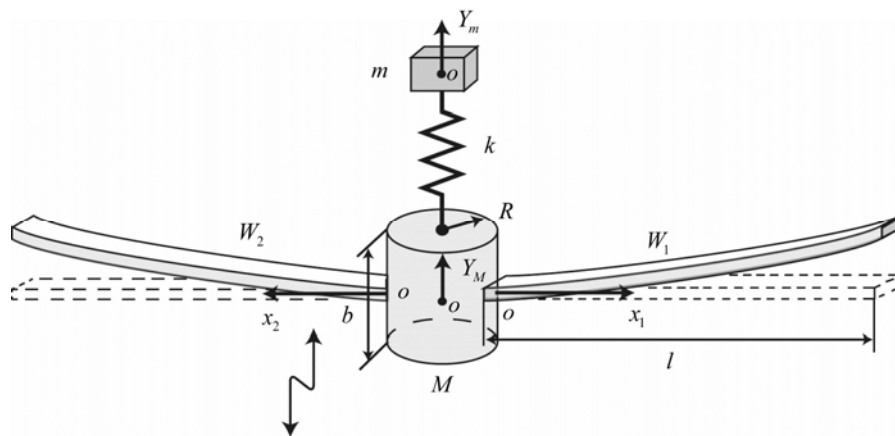


Fig. 1 Flexible spacecraft with liquid tank

rigid tank under low gravity would be a serious problem. Buzhinskii (2009) studied the effect of sloshing on the rocket motion modelling it as a thin-walled structure with a liquid. Recently Farhat *et al.* (2013) investigated fuel sloshing effect on the spacecraft and its flutter characteristics.

In the present study, as the first step toward clarifying the fundamental vibration characteristics of flexible space structures with on-board liquid, we propose a mechanical model and theoretically analyze the axisymmetric coupled vibrations of a flexible structure with on-board liquid in zero gravity environments. In the proposed model, the main body is modeled as a rigid mass, the flexible appendages as two elastic beams, and on-board liquid as a “spring-mass” system (mechanical model). In the mechanical model, as we adopt single liquid sloshing mode, i.e., fundamental sloshing mode, we can grasp just broad vibration characteristics of the coupled system, i.e., main body-flexible appendages-liquid system. The present paper is a basic study of the foregoing one in which liquid is considered as an ideal liquid with meniscus of free surface which will be presented as Part II of the paper.

## 2. Basic equation and boundary condition

### 2.1 Analytical model

We shall consider the free vibration of a spacecraft, as shown in Fig. 1, which has flexible appendages such as solar arrays on both sides of the main body and liquid on board. The spacecraft’s main body is modeled as a rigid mass, the flexible appendages as two elastic beams, and the on-board liquid as a “spring-mass” system.

The beams are uniform *Euler-Bernoulli* beams with cross-sectional area  $A$ , density  $\rho_b$ , Young’s modulus  $E$ , second moment of area  $I$ , while the “spring-mass” system, which represents liquid on board, has mass  $m$  (hereafter, we call it added mass) and spring constant  $k$ . We assume that two beams are arranged symmetrically with respect to the rigid mass and the mass center of rigid mass lies in the mid-surface of two beams, which enable axisymmetric in-plane motion, i.e., movement along only the upward and downward directions in the plane of the figure.

The displacements of the main rigid mass  $M$  and the added mass  $m$  are  $Y_M$  and  $Y_m$ , respectively. Additionally, the beams are clamped with the rigid mass  $M$ , and their displacements are  $W_1(x_1, t)$  and  $W_2(x_2, t)$ , respectively, at  $x_1$  and  $x_2$  from the clamped origin.

### 2.2 Basic equation

The kinetic energy  $T$  of the system consists of the kinetic energies of the two beams, added mass, and main rigid mass as follows

$$T = \frac{\rho_b A}{2} \int_0^l (\dot{W}_1(x_1, t))^2 dx_1 + \frac{\rho_b A}{2} \int_0^l (\dot{W}_2(x_2, t))^2 dx_2 + \frac{1}{2} m \dot{Y}_m^2 + \frac{1}{2} M \dot{Y}_M^2 \quad (1)$$

And the potential energy  $U$  consists of the beams’ bending strain energies and the “spring-mass” system’s strain energy.

$$U = \frac{EI}{2} \int_0^l \left( \frac{\partial^2 W_1(x_1, t)}{\partial x_1^2} \right)^2 dx_1 + \frac{EI}{2} \int_0^l \left( \frac{\partial^2 W_2(x_2, t)}{\partial x_2^2} \right)^2 dx_2 + \frac{1}{2} k (Y_m - Y_M)^2 \quad (2)$$

Therefore, the *Lagrangian* of the system is as follows

$$\begin{aligned}
 L &= T - U \\
 &= \frac{\rho_b A}{2} \int_0^l (\dot{W}_1(x_1, t))^2 dx_1 + \frac{\rho_b A}{2} \int_0^l (\dot{W}_2(x_2, t))^2 dx_2 + \frac{1}{2} m \dot{Y}_m^2 + \frac{1}{2} M \dot{Y}_M^2 \\
 &\quad - \frac{EI}{2} \int_0^l \left( \frac{\partial^2 W_1(x_1, t)}{\partial x_1^2} \right)^2 dx_1 - \frac{EI}{2} \int_0^l \left( \frac{\partial^2 W_2(x_2, t)}{\partial x_2^2} \right)^2 dx_2 - \frac{1}{2} k (Y_m - Y_M)^2
 \end{aligned} \tag{3}$$

Assuming that the system undergoes a small-amplitude harmonic motion with circular frequency  $\omega$  as follows

$$\begin{aligned}
 Y_m(t) &= y_m \cos \omega t \\
 Y_M(t) &= y_M \cos \omega t
 \end{aligned} \tag{4}$$

$$W_i(x_i, t) = w_i(x_i) \cos \omega t, \quad i = 1, 2$$

Here, the following non-dimensional parameters are introduced,

$$\begin{aligned}
 \tau = \omega_b t, \quad \xi_i = \frac{x_i}{l}, \quad \bar{w}_i = \frac{w_i}{l}, \quad \zeta = \frac{y_m}{l}, \quad \eta = \frac{y_M}{l}, \quad \Omega = \frac{\omega}{\omega_b}, \quad \omega_b = \sqrt{\frac{EI}{\rho_b Al^4}} \\
 \bar{M} = \frac{M}{2\rho_b Al}, \quad \bar{m} = \frac{m}{2\rho_b Al}, \quad \kappa = \frac{kl^3}{EI}
 \end{aligned} \tag{5}$$

where  $\bar{M}$  is the ratio of mass  $M$  to the mass of two beams  $2\rho_b Al$ , “mass ratio,”  $\bar{m}$  is the ratio of the added mass  $m$  to the mass of two beams  $2\rho_b Al$ , “added mass ratio,”  $\kappa$  is the ratio of spring constant  $k$  to the bending rigidity of the beams, “spring rigidity.”

Using Eqs. (4) and (5), Eq. (3) can be written as follows

$$\begin{aligned}
 \bar{L} &= L \left( \frac{2l}{EI} \right) \\
 &= \Omega^2 \int_0^1 \bar{w}_1^2(\xi_1) d\xi_1 \sin^2 \Omega \tau + \Omega^2 \int_0^1 \bar{w}_2^2(\xi_2) d\xi_2 \sin^2 \Omega \tau + 2\Omega^2 \bar{m} \zeta^2 \sin^2 \Omega \tau + 2\Omega^2 \bar{M} \eta^2 \sin^2 \Omega \tau \\
 &\quad - \int_0^1 \left( \frac{d^2 \bar{w}_1(\xi_1)}{d\xi_1^2} \right)^2 d\xi_1 \cos^2 \Omega \tau - \int_0^1 \left( \frac{d^2 \bar{w}_2(\xi_2)}{d\xi_2^2} \right)^2 d\xi_2 \cos^2 \Omega \tau - \kappa (\zeta - \eta)^2 \cos^2 \Omega \tau
 \end{aligned} \tag{6}$$

Integrating this equation with respect to non-dimensional time  $\tau$  for one period of vibration,  $0 \sim 2\pi / \Omega$

$$\int_0^{\frac{2\pi}{\Omega}} \sin^2 \Omega \tau d\tau = \int_0^{\frac{2\pi}{\Omega}} \cos^2 \Omega \tau d\tau = \frac{\pi}{\Omega} \tag{7}$$

we obtain the *Lagrangian* of the system as

$$\begin{aligned} \bar{L} &= \int_0^{2\pi} \bar{L} d\tau \\ &= \pi \Omega \int_0^1 \bar{w}_1^2(\xi_1) d\xi_1 + \pi \Omega \int_0^1 \bar{w}_2^2(\xi_2) d\xi_2 + 2\pi \Omega \bar{m} \zeta^2 + 2\pi \Omega \bar{M} \eta^2 \\ &\quad - \frac{\pi}{\Omega} \int_0^1 \left( \frac{d^2 \bar{w}_1(\xi_1)}{d\xi_1^2} \right)^2 d\xi_1 - \frac{\pi}{\Omega} \int_0^1 \left( \frac{d^2 \bar{w}_2(\xi_2)}{d\xi_2^2} \right)^2 d\xi_2 - \frac{\pi}{\Omega} \kappa (\zeta - \eta)^2 \end{aligned} \tag{8}$$

$$\begin{aligned} \tilde{L} &= \bar{L} \frac{\Omega}{\pi} \\ &= \Omega^2 \int_0^1 \bar{w}_1^2(\xi_1) d\xi_1 + \Omega^2 \int_0^1 \bar{w}_2^2(\xi_2) d\xi_2 + 2\Omega^2 \bar{m} \zeta^2 + 2\Omega^2 \bar{M} \eta^2 \\ &\quad - \int_0^1 \left( \frac{d^2 \bar{w}_1(\xi_1)}{d\xi_1^2} \right)^2 d\xi_1 - \int_0^1 \left( \frac{d^2 \bar{w}_2(\xi_2)}{d\xi_2^2} \right)^2 d\xi_2 - \kappa (\zeta - \eta)^2 \end{aligned} \tag{9}$$

### 2.3 Method of solution

Firstly, beam deflections are assumed to be of the following form

$$\bar{w}_1(\xi_1) = \sum_m a_m \tilde{w}_{1m}(\xi_1), \quad \bar{w}_2(\xi_2) = \sum_n b_n \tilde{w}_{2n}(\xi_2) \tag{10}$$

where  $a_m$  and  $b_n$  are unknown constants and  $\tilde{w}_{im}(\xi_i) : i=1, 2$  is an eigenfunction of the beam with “mass-free” boundary conditions, i.e., at  $x=0$ , the shearing force of the beam is balanced with inertia force of mass  $M/2$ , and the deflection angle is zero, and at  $x=l$ , the shearing force and bending moment are zero as follows

$$\begin{aligned} -\frac{1}{2} M \ddot{Y}_M(t) - EI \frac{\partial^3 w_i(x_i, t)}{\partial x_i^3} = 0, \quad \frac{\partial w_i(x_i, t)}{\partial x_i} = 0 & \quad \text{at } x_i = 0 \\ -EI \frac{\partial^3 w_i(x_i, t)}{\partial x_i^3} = 0, \quad -EI \frac{\partial^2 w_i(x_i, t)}{\partial x_i^2} = 0 & \quad \text{at } x_i = l \end{aligned} \tag{11}$$

In the non-dimensional form

$$\begin{aligned} \frac{\partial^3 \bar{w}_i}{\partial \xi_i^3} = \Omega^2 \bar{M} \eta, \quad \frac{\partial \bar{w}_i}{\partial \xi_i} = 0 & \quad \text{at } \xi_i = 0 \\ \frac{\partial^3 \bar{w}_i}{\partial \xi_i^3} = 0, \quad \frac{\partial^2 \bar{w}_i}{\partial \xi_i^2} = 0 & \quad \text{at } \xi_i = 1 \end{aligned} \tag{12}$$

The eigenfunction that satisfies the above boundary conditions is written as follows

$$\tilde{w}_{im}(\xi_i) = C_m \left\{ \cosh \alpha_m \xi + \frac{1}{2} \bar{M} \alpha_m (\sinh \alpha_m \xi_i - \sin \alpha_m \xi_i) \right. \\ \left. - \frac{\sinh \alpha_m + \frac{1}{2} \bar{M} \alpha_m (\cos \alpha_m + \cosh \alpha_m)}{\sin \alpha_m + \frac{1}{2} \bar{M} \alpha_m (\cos \alpha_m + \cosh \alpha_m)} \left( \cos \alpha_m \xi_i + \frac{1}{2} \bar{M} \alpha_m (\sinh \alpha_m \xi_i - \sin \alpha_m \xi_i) \right) \right\} \quad (13)$$

where  $\alpha_m$  is a parameter that satisfies the following frequency equation and is presented in Appendix A.

$$\sinh \alpha_m \cos \alpha_m + \cosh \alpha_m \sin \alpha_m + \bar{M} \alpha_m (1 + \cos \alpha_m \cosh \alpha_m) = 0 \quad (14)$$

Eigenfunction  $\tilde{w}_{im}(\xi_i)$  has following characteristics in its integration

$$X_{mn}^{00} = \int_0^1 \tilde{w}_{im}(\xi_i) \tilde{w}_{in}(\xi_i) d\xi_i = \begin{cases} -\bar{M} \tilde{w}_{in}(0) \tilde{w}_{im}(0) & : m \neq n \\ \frac{1}{4} (\tilde{w}_{in}^2(1) - 3\bar{M} \tilde{w}_{in}^2(0)) & : m = n \end{cases} \quad (15)$$

$$X_{mn}^{22} = \int_0^1 \frac{d^2 \tilde{w}_{im}(\xi_i)}{d\xi_i^2} \frac{d^2 \tilde{w}_{in}(\xi_i)}{d\xi_i^2} d\xi_i = \begin{cases} 0 & : m \neq n \\ \frac{1}{4} \alpha_n^4 (\tilde{w}_{in}^2(1) + \bar{M} \tilde{w}_{in}^2(0)) & : m = n \end{cases} \quad (16)$$

Substituting Eq. (10) into Eq. (9), we obtain the following

$$\tilde{L} = \Omega^2 \sum_m \sum_n a_m a_n \int_0^1 \tilde{w}_{1m}(\xi_1) \tilde{w}_{1n}(\xi_1) d\xi_1 + \Omega^2 \sum_m \sum_n b_m b_n \int_0^1 \tilde{w}_{2m}(\xi_2) \tilde{w}_{2n}(\xi_2) d\xi_2 \\ + 2\Omega^2 \bar{m} \zeta^2 + 2\Omega^2 \bar{M} \eta^2 \\ - \sum_m \sum_n a_m a_n \int_0^1 \frac{d^2 \tilde{w}_{1m}(\xi_1)}{d\xi_1^2} \frac{d^2 \tilde{w}_{1n}(\xi_1)}{d\xi_1^2} d\xi_1 - \sum_m \sum_n b_m b_n \int_0^1 \frac{d^2 \tilde{w}_{2m}(\xi_2)}{d\xi_2^2} \frac{d^2 \tilde{w}_{2n}(\xi_2)}{d\xi_2^2} d\xi_2 \\ - \kappa (\zeta - \eta)^2 \quad (17)$$

Using Eqs. (15) and (16), we get the following expression

$$\tilde{L} = \Omega^2 \sum_m \sum_n a_m a_n X_{mn}^{00} + \Omega^2 \sum_m \sum_n b_m b_n X_{mn}^{22} + 2\Omega^2 \bar{m} \zeta^2 + 2\Omega^2 \bar{M} \eta^2 \\ - \sum_m \sum_n a_m a_n X_{mn}^{22} - \sum_m \sum_n b_m b_n X_{mn}^{22} - \kappa (\zeta - \eta)^2 \quad (18)$$

Here, assuming that the two beams are identical, i.e.,  $b_m = a_m$

$$\tilde{L} = 2\Omega^2 \sum_m \sum_n a_m a_n X_{mm}^{00} + 2\Omega^2 \bar{m} \zeta^2 + 2\Omega^2 \bar{M} \eta^2 - 2 \sum_m \sum_n a_m a_n X_{mm}^{22} - \kappa (\zeta - \eta)^2 \quad (19)$$

Displacements of the main body and the clamped ends of the beams must be equal

$$y_M = w_i(0): i = 1, 2 \tag{20a}$$

in the non-dimensional form.

$$\eta = \bar{w}_i(0): i = 1, 2 \tag{20b}$$

From Eqs. (10) and (20b),  $\eta$  can be represented in terms of  $a_m$  as follows

$$\eta = \sum_m a_m \tilde{w}_m(0) \tag{21}$$

Substituting this into Eq. (19), we get the following expression

$$\begin{aligned} \tilde{L} = & 2\Omega^2 \sum_m \sum_n a_m a_n X_{mn}^{00} + 2\Omega^2 \bar{m} \zeta^2 + 2\Omega^2 \bar{M} \left( \sum_m a_m \tilde{w}_{1m}(0) \right)^2 \\ & - 2 \sum_m \sum_n a_m a_n X_{mn}^{22} - \kappa \left( \zeta - \sum_m a_m \tilde{w}_{1m}(0) \right)^2 \end{aligned} \tag{22}$$

Thus far, the *Lagrangian*  $\tilde{L}$  can be represented in terms of  $a_m$  and  $\zeta$ .

Here applying *Rayleigh-Ritz* method, we obtain the following minimalized condition for  $\tilde{L}$ :

$$\frac{\partial \tilde{L}}{\partial a_m} = 0, \quad \frac{\partial \tilde{L}}{\partial \zeta} = 0$$

$$\begin{aligned} \frac{\partial \tilde{L}}{\partial a_m} = & 4\Omega^2 \left( \sum_n a_n X_{mn}^{00} + \bar{M} \tilde{w}_m(0) \sum_n a_n \tilde{w}_n(0) \right) \\ & - 4 \sum_n a_n X_{mn}^{22} - 2\kappa \left( -\zeta \tilde{w}_m(0) + \tilde{w}_m(0) \sum_n a_n \tilde{w}_n(0) \right) = 0 \end{aligned} \tag{23}$$

$$\frac{\partial \tilde{L}}{\partial \zeta} = 4\Omega^2 \bar{m} \zeta - 2\kappa \left( \zeta - \sum_m a_m \tilde{w}_m(0) \right) = 0$$

The above equation can be represented as the following matrix form

$$\left[ \begin{array}{cc} \bar{\mathbf{X}}^{22} & -\frac{1}{2} \kappa \tilde{\mathbf{w}}^T \\ -\frac{1}{2} \kappa \tilde{\mathbf{w}} & \frac{1}{2} \kappa \end{array} \right] - \Omega^2 \left[ \begin{array}{cc} \bar{\mathbf{X}}^{00} & \mathbf{0} \\ \mathbf{0} & \bar{m} \end{array} \right] \begin{Bmatrix} \mathbf{a} \\ \zeta \end{Bmatrix} = \begin{Bmatrix} \mathbf{0} \\ 0 \end{Bmatrix} \tag{24}$$

where

$$\bar{X}_{mn}^{22} = X_{mn}^{22} + \frac{1}{2} \kappa \tilde{w}_m(0) \tilde{w}_n(0)$$

$$\bar{X}_{mn}^{00} = X_{mn}^{00} + \bar{M} \tilde{w}_m(0) \tilde{w}_n(0)$$

Eq. (24) is a coupled equation in terms of  $a_m$  and  $\zeta$ , and the problem can be reduced into an eigenvalue problem from which one can obtain the coupled natural circular frequencies as eigenvalues and the vibration modes as eigenvectors.

### 3. Numerical results

Currently, coupled dynamic systems are represented by three system parameters, i.e., the mass ratio  $\bar{M}$ , added mass ratio  $\bar{m}$ , and spring rigidity parameter  $\kappa$ . Variation ranges of the former two system parameters,  $\bar{M}$  and  $\bar{m}$ , were analogized as  $\bar{M} = 1 - 200$  and  $\bar{m} = 0.5 - 100$  considering the specifications of some application satellites (see Appendix B).

#### 3.1 “Spring-two masses” system

First, before proceeding to the coupled vibration system consisting of three elements, i.e., the rigid mass (main body), spring-added mass (liquid), and elastic beams (flexural appendages), we consider a “spring-two masses” system in which the flexible beams are assumed to be rigid beams, as shown in Fig. 2(b). The “spring-two masses” system can be regarded as a satellite when its paddles are folded. A comparison of the natural frequencies of the original coupled system and those of the “spring-two masses” system indicates that the “spring-two masses” system has significance in demonstrating the effect of beam flexibility.

Equations of motion for mass  $m$  and  $M + 2\rho Al$ , shown in Fig. 2(b), are as follows

$$-m\ddot{Y}_m - k(Y_m - Y_M) = 0 \quad (25a)$$

$$-(M + 2\rho AL)\ddot{Y}_M - k(Y_M - Y_m) = 0 \quad (25b)$$

From these equations, we obtain the natural circular frequency, hereafter, we simply call it “natural frequency” of the “spring-two masses” system, i.e., two masses bounded with a spring and freely floating in space.

$$\omega = \sqrt{\frac{k(m + M + 2\rho AL)}{m(M + 2\rho AL)}} \quad (26)$$

The non-dimensional form of Eq. (26) is as follows

$$\Omega = \sqrt{\frac{\kappa(\bar{m} + \bar{M} + 1)}{2\bar{m}(\bar{M} + 1)}} \quad (27)$$

The natural frequencies of the “spring-two masses” system are shown in Figs. 3 and 4. Fig. 3(a) shows variations in the natural frequency  $\Omega$  with variations in the added mass ratio  $\bar{m}$ ; in the figure, the black, blue, and brown lines represent situations in which spring rigidity is  $\kappa = 1$ ,  $\kappa = 10$ ,  $\kappa = 100$ , respectively, while the dotted, broken, and solid lines represent situations in

which mass ratio is  $\bar{M} = 1$ ,  $\bar{M} = 10$ ,  $\bar{M} = 100$ , respectively. From the figure, we find that as  $\bar{m}$  increases, the natural frequency decreases gradually and approaches a value that depends on the mass ratio  $\bar{M}$ . In contrast, as  $\bar{m}$  decreases, the natural frequency increases and approaches a value that is not dependent on  $\bar{M}$  but dependent on  $\kappa$ .

Fig. 3(b) shows variations in  $\Omega$  with the mass ratio  $\bar{M}$ , and the results corresponding to  $\bar{m} = 1$ ,  $\bar{m} = 10$ , and  $\bar{m} = 100$  are represented by the single-dotted, dashed, and solid lines, respectively. As  $\bar{M}$  increases, the natural frequency decreases and approaches a value that depends on  $\kappa$  and  $\bar{m}$ , and the natural frequency with larger  $\bar{m}$  is lower compared to that with the same value of  $\bar{M}$ .

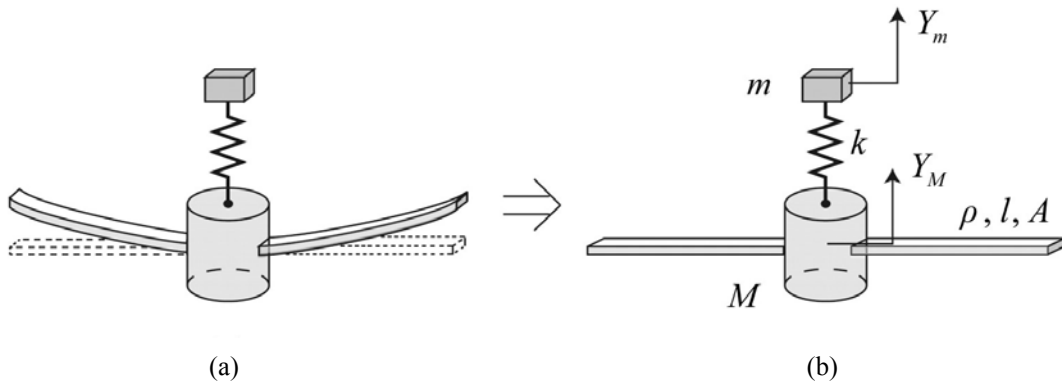


Fig. 2 (a) Mechanical model; (b) Spring-two masses model

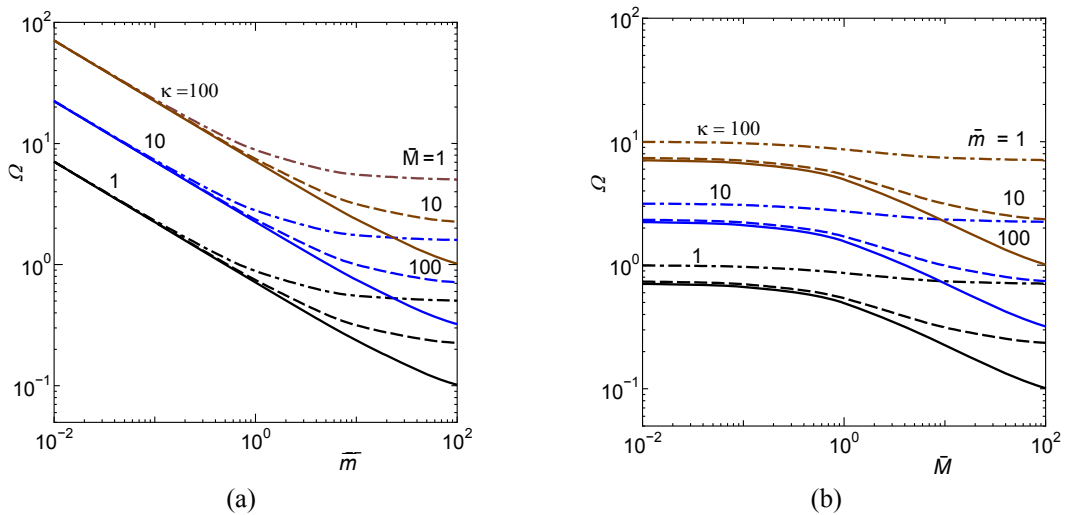


Fig. 3 Natural frequency of “spring - two masses model”: ( $\kappa = 1, 10, 100$ ); (a) Variation with  $\bar{m}$ ; (b) Variation with  $\bar{M}$

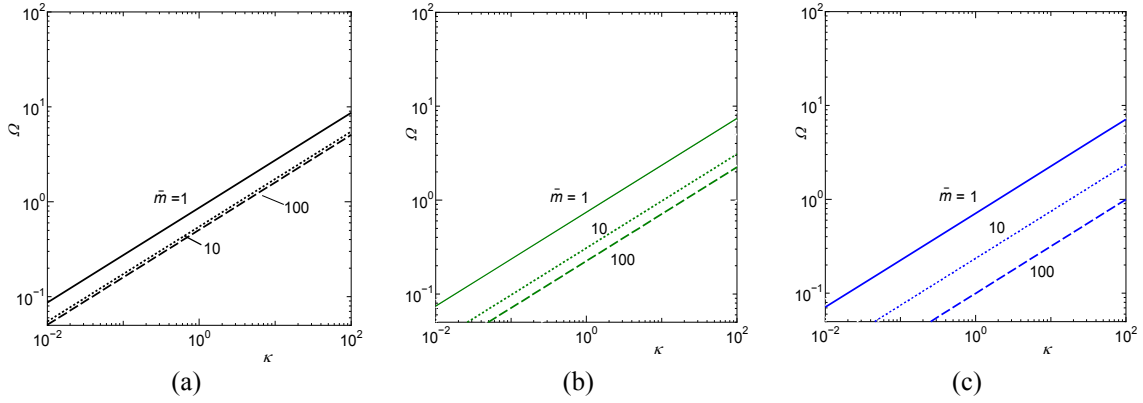


Fig. 4 Natural frequency of “spring - two masses model”: Influence of spring rigidity  $\kappa$ ; (a)  $\bar{M} = 1$ ; (b)  $\bar{M} = 10$ ; (c)  $\bar{M} = 100$

Fig. 4 shows that the natural frequency is proportional to  $\kappa$ , and with an increase in  $\bar{m}$ , the natural frequency decreases; this tendency is stronger for larger values of  $\bar{M}$ .

### 3.2 Free-free beam with central mass

Next, we consider a free-free beam with a mass at its center, as shown in Fig. 5(b). This model does not include the added mass and spring, which represent the on-board liquid. This is a model of the satellite main body with flexural appendages and an empty fuel tank and has potential for demonstrating the effect of liquid sloshing.

In this case, neglecting the term concerned with the added mass (liquid) from Eq. (24), one obtains the following expression

$$\left\{ \bar{\mathbf{X}}_{mn}^{22} - \Omega^2 \bar{\mathbf{X}}_{mn}^{00} \right\} \{ \mathbf{a} \} = \mathbf{0} \tag{28}$$

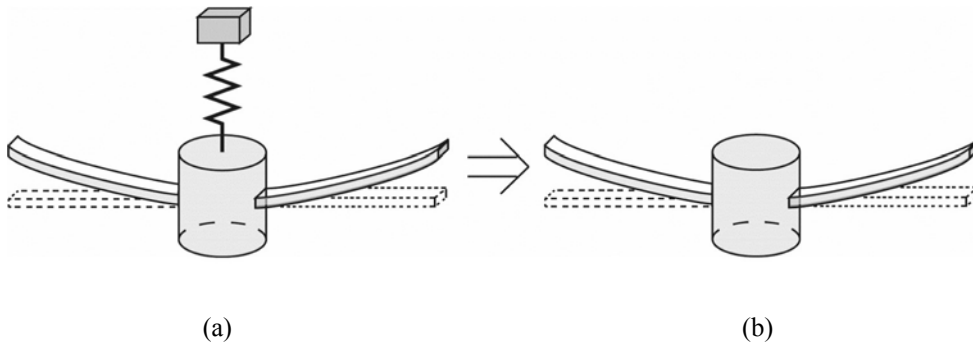


Fig. 5 (a) Mechanical model; (b) Elastic beam with central mass model

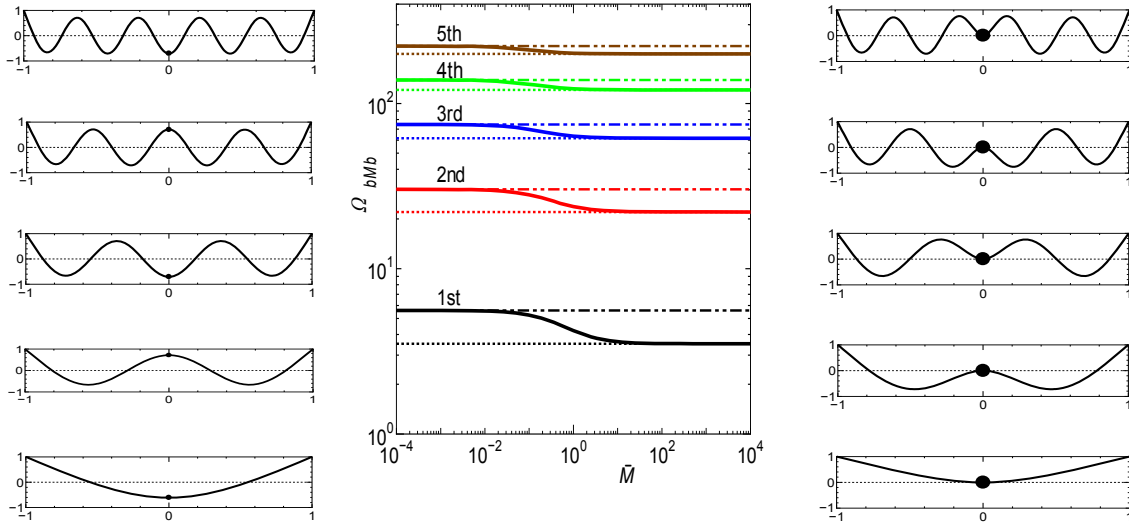


Fig. 6 Variations in natural frequencies and vibration modes of a beam with central mass  $\bar{M}$

Given that these are the uncoupled frequency equations, one can obtain the natural frequency  $\Omega_{bMb}$  as follows

$$\Omega_{bMb} = \alpha_k^2 \tag{29}$$

Variation in  $\Omega_{bMb}$  with variations in  $\bar{M}$  corresponding to the vibration modes when  $\bar{M} = 10^{-4}$  and  $10^4$  are shown in Fig. 6. As  $\bar{M}$  tends to zero ( $\bar{M} \rightarrow 0$ ),  $\Omega_{bMb}$  approaches the natural frequencies of the odd mode of the free-free beam having a non-dimensional length of 2,  $\Omega_{2FF}$  (see Table A3 in Appendix C), which is represented by two dotted lines in the figure. Corresponding vibration modes are presented in the left hand side of the diagram. In contrast, as  $\bar{M}$  tends to infinity ( $\bar{M} \rightarrow \infty$ ), deflection of the beam center decreases and  $\Omega_{bMb}$  approaches the natural frequencies of a cantilever beam,  $\Omega_{CF}$  (see Table A4 in Appendix C), which is represented by dotted lines in the figure. Corresponding vibration modes are presented in the right hand side of the diagram. From these, the correctness of the present results can be verified in some parts.

Fig. 7 shows variations of the vibration mode when  $\bar{M} = 0, 1, 10, 100$ . From this figure, one can see that with an increase in  $\bar{M}$ , deflection at the beam center decreases to zero. In other words, when the main mass  $\bar{M}$  is small, the influence of beam vibration on the main body is significant, and the motion of the main body is not zero.

### 3.3 Coupled system

#### 3.3.1 Effect of spring rigidity $\kappa$

Finally, we consider a coupled system. Fig. 8 shows variations of the coupled natural frequencies with  $\bar{m}$  for  $\bar{M} = 10$  and  $\kappa = 0.1, 1, 10, 100$ . In the figure, the coupled frequencies are represented by solid lines, those of the “spring-two mass” system obtained in 3.1 are

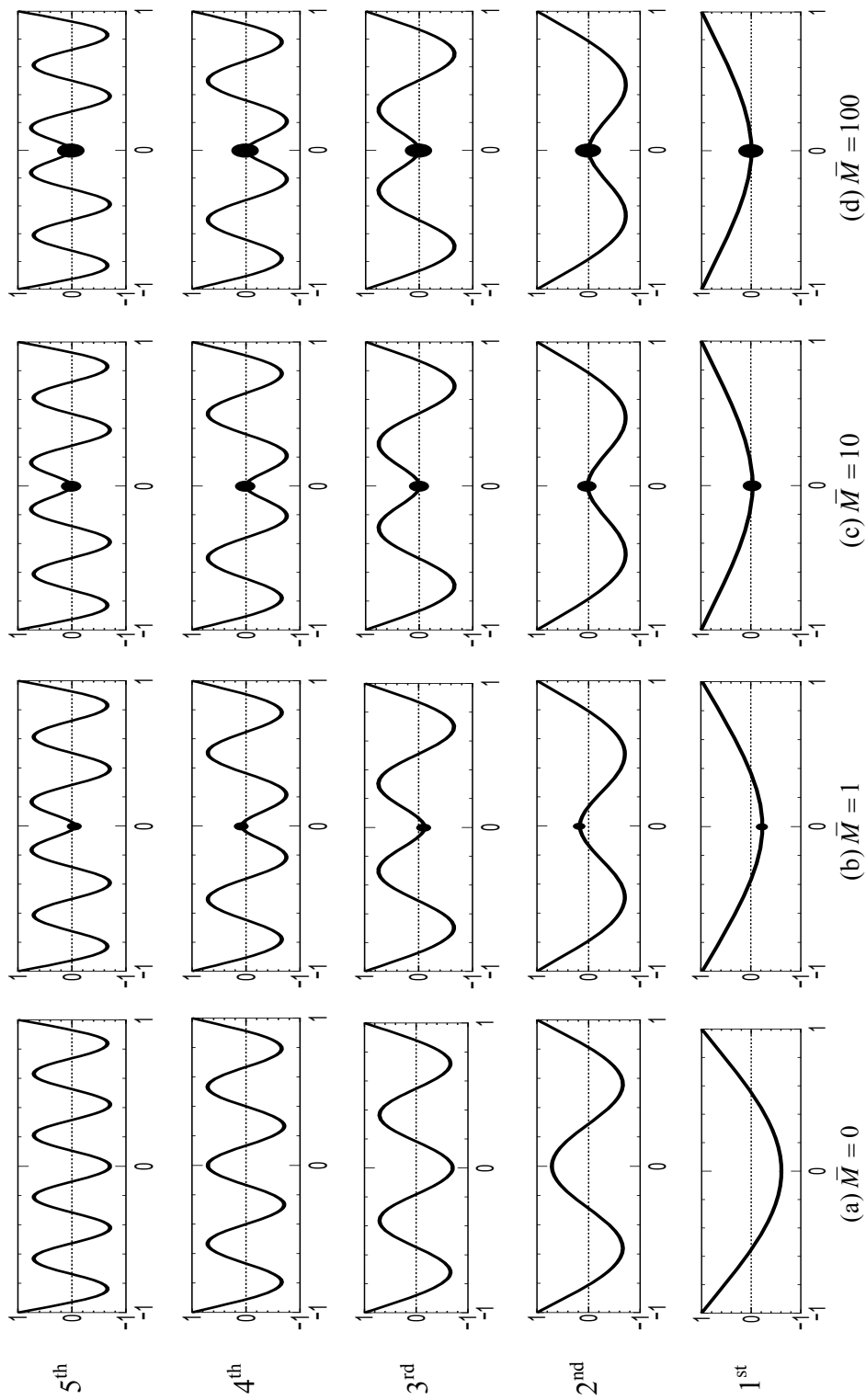


Fig. 7 Vibration modes of a beam with central mass  $\bar{M}$ ; (a)  $\bar{M} = 0$ ; (b)  $\bar{M} = 1$ ; (c)  $\bar{M} = 10$ ; (d)  $\bar{M} = 100$

represented by dashed lines, and those of the beam with central mass obtained in 3.2 are represented by single-dotted lines. Detailed relationships among these three frequencies are discussed in the next section.

When  $\kappa = 0.1$ , as shown in Fig. 8(a), one can find two types of coupled natural frequencies, one of which decreases with  $\bar{m}$ , and the other nearly constant with  $\bar{m}$ . The former follows frequency curves of the “spring-two masses” system, indicated by dashed lines, in which the added mass (liquid) motion is predominant. The latter follows the frequency curves of “the beam with central mass,” represented by single-dotted lines, in which the beam motion is predominant. Hereafter, we shall call the former coupled frequency as “coupled added mass frequency” and the latter as “coupled beam frequency,” respectively. In this case, there seems to be no crossing or veering of the frequency curves in this region of  $\bar{m}$ , i.e., there is no coupling between these two types of vibrations.

When the spring rigidity increases to  $\kappa = 1$ , as shown in Fig. 8(b), compared with  $\kappa = 0.1$  case, the coupled added mass frequency increases over the  $\bar{m}$  range, and the frequency curve of this mode crosses that of the first coupled bending mode of the beam near the  $\bar{m} = 0.03$  region. In this region, coupling between the first bending motion of the beam and the added mass motion seems to be strong. However, it should be noted here, that although the two curves appear to intersect, they are actually simply veering toward each other, and the two frequency curves in which the beam motion and the added mass motion are predominant become interchanged, as is shown later.

When  $\kappa = 10$ , as in Fig. 8(c), the coupled added mass frequency increases further, and this frequency curve approaches that of the coupled second beam mode near the  $\bar{m} = 0.01$  region. In comparison with the case in which  $\kappa = 1$ , the value of  $\bar{m}$  at which coupling occurs with the beam mode increases.

When  $\kappa = 100$ , as in Fig. 8(d), any further increase in the coupled added mass frequency leads to coupling with the third beam mode in the  $\bar{m} = 0.01$  region. In addition, the value of  $\bar{m}$  at which coupling with the second beam mode takes place increases to  $\bar{m} = 0.1$ , and that at which coupling with the 1<sup>st</sup> beam mode takes place increases to  $\bar{m} = 4$ . In each case, as  $\bar{m}$  increases, the lowest coupled natural frequency, indicated by red curve, separates from that of the “spring-two mass” system, which is represented by the dashed line. This is because in the former case, we assume that the beam is elastic, whereas, in the latter case, we assume that it is rigid; therefore, the coupled natural frequency of the former case is lower than that of the latter case.

Thus far, the followings are summarized.

- There are two vibration types in the coupled system: that in which beam motion is predominant and that corresponds to the motion of the added mass (liquid).
- As  $\bar{m}$  increases, the coupled added mass frequency decreases.
- As  $\kappa$  increases, the coupled added mass frequency increases over the parameter range of  $\bar{m}$ , which leads to increases in the number of couplings with the beam modes as well as in the value of  $\bar{m}$ .
- In actual spacecraft, as fuel is consumed step by step, i.e.,  $\bar{m}$  decreases gradually, at some fuel mass  $\bar{m}$ , the sloshing frequency approaches one of the flexural structure frequencies and strong coupled motion is expected to occur. For lower  $\bar{m}$ , coupling occurs with the structural modes of higher orders.

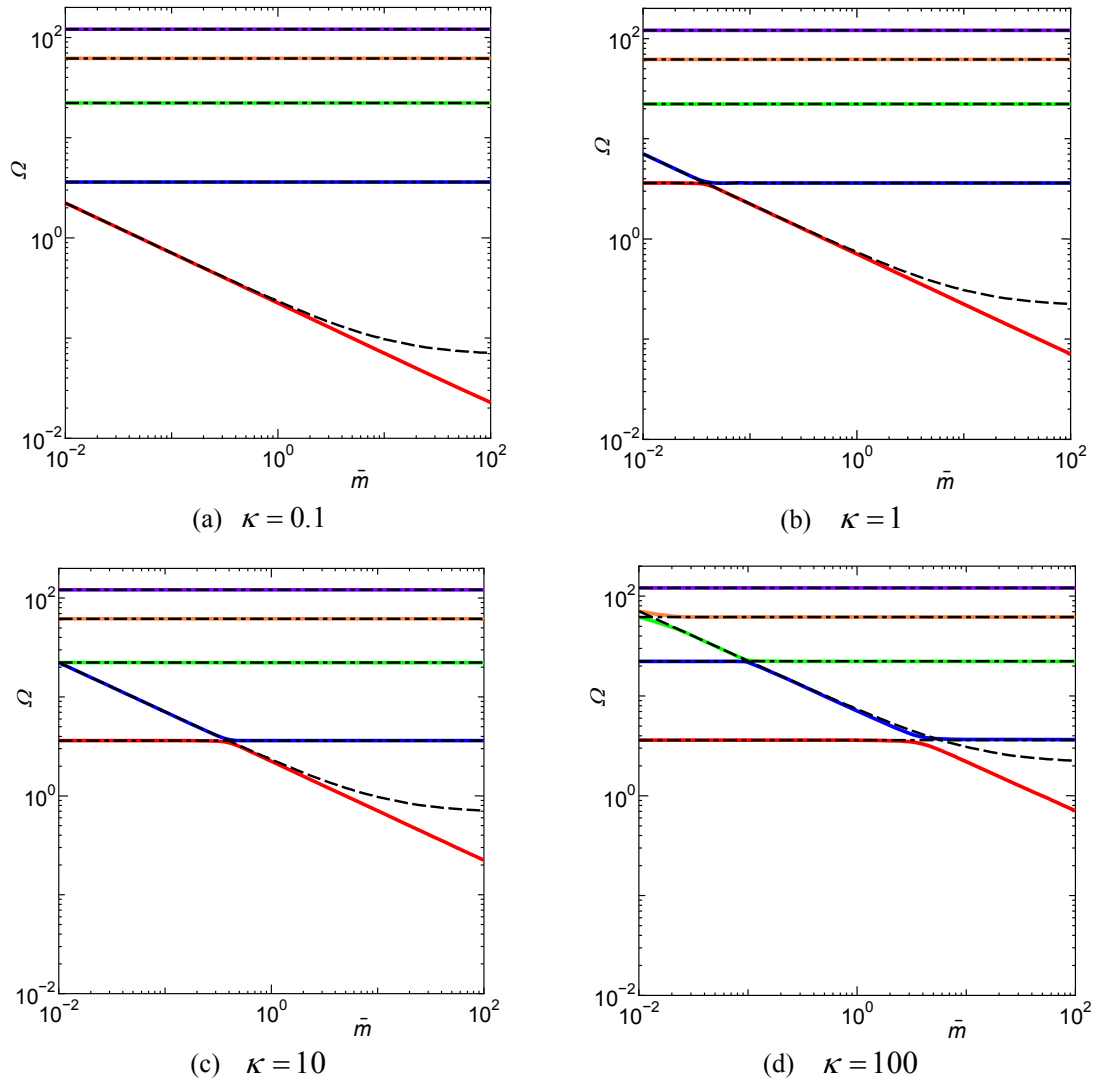


Fig. 8 Coupled natural frequencies with added mass ratio  $\bar{m} : \bar{M} = 10$ ; (a)  $\kappa = 0.1$ ; (b)  $\kappa = 1$ ; (c)  $\kappa = 10$ ; (d)  $\kappa = 100$

### 3.3.2 Effect of main mass ratio $\bar{M}$

Next, we examine the effect of the main mass ratio  $\bar{M}$ . The coupled natural frequencies are shown in Fig. 9 for  $\bar{M} = 0, 1, 10, 100$  and  $\kappa = 100$ . As mentioned above, when sets  $\bar{m}$  as the abscissa, there are two types of coupled frequency curves: the one in which liquid motion is predominant, represented by the curve that slopes downward with  $\bar{m}$ , and the other in which the beam motion is predominant, represented by the curve that is nearly constant with  $\bar{m}$ . As shown in Fig. 6, for the uncoupled natural frequency variations with  $\bar{M}$  of the latter type, the natural frequency decreases gradually and the rate of decrease is large in the  $\bar{M} = 0.01 \sim 10$  region; however, this frequency variation is very small and cannot be recognized in Fig. 9.

For the former type of coupled frequency, given that the liquid motion influences the main body when  $\bar{M}$  is small, vibration is generated easily in the beams that are rigidly connected to the main body, and the coupling region in the figure widens, as shown in Figs. 9(a) and (b). As  $\bar{M}$  increases, i.e., the mass of the main body increases, the influence of the liquid motion on the main body decreases gradually, which ensures that the beam is not excited and the coupling region becomes narrower, as shown in Figs. 9(c) and (d).

From these results, one can deduce the situation in the actual spacecraft

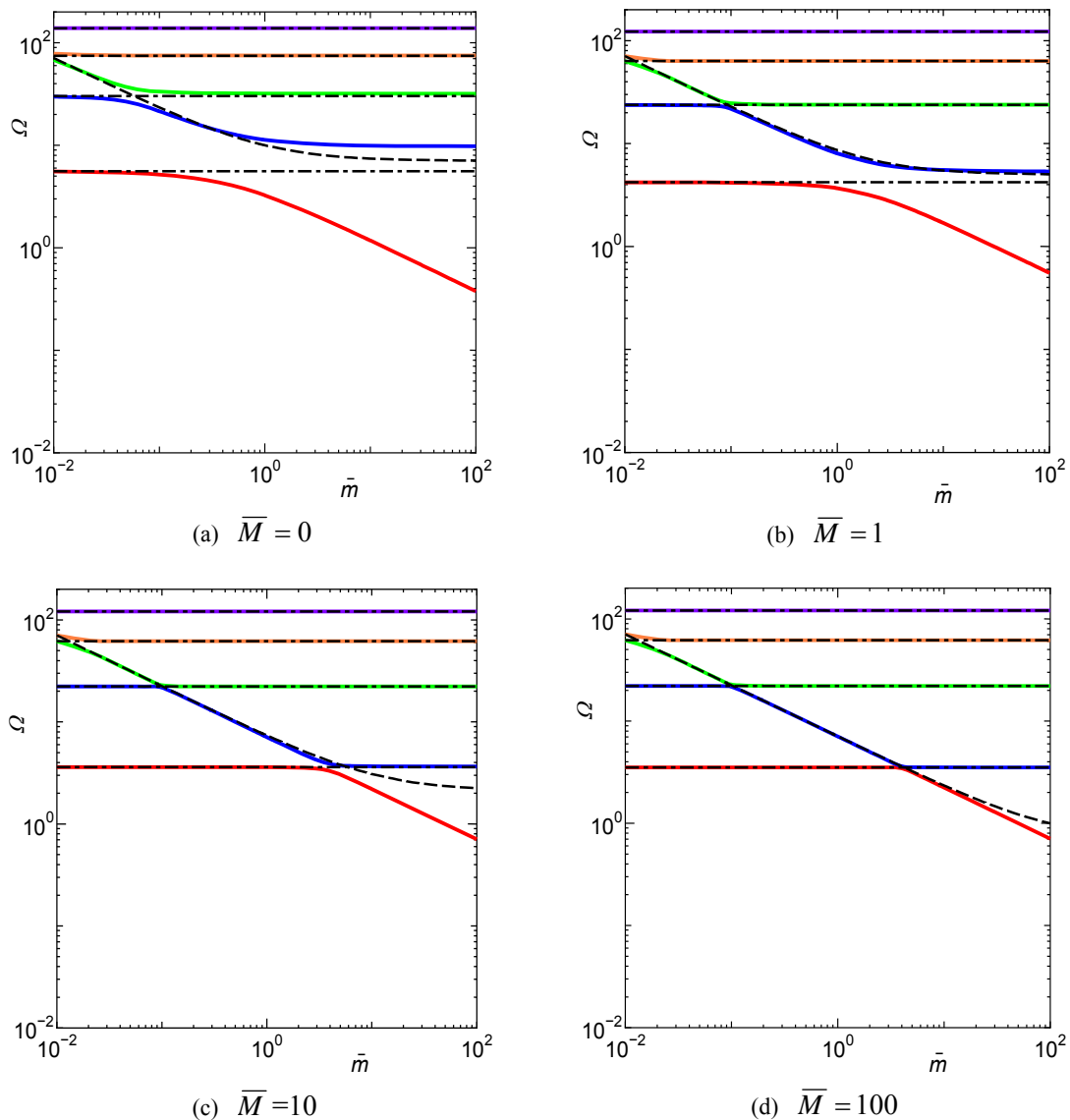


Fig. 9 Coupled natural frequencies with added mass ratio  $\bar{m} : \kappa = 100$ ; (a)  $\bar{M} = 0$ ; (b)  $\bar{M} = 1$ ; (c)  $\bar{M} = 10$ ; (d)  $\bar{M} = 100$

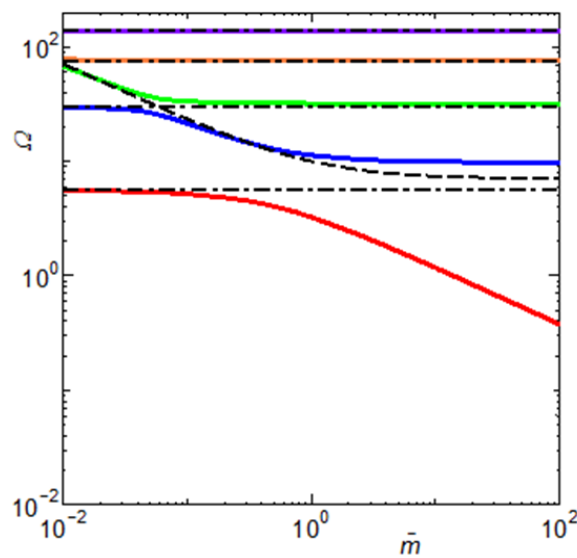
- When the mass of the main body is small, the influence of liquid sloshing motion on the main body is significant. Therefore, vibration in the appendages connected to the main body is generated easily, thus leading to a wider coupling region, as shown in Figs. 9(a) and (b).
- When the mass of the main body is large, the influence of the liquid sloshing motion is small; then, it is difficult to generate vibration in the appendages, and the coupling region becomes narrow, as shown in Figs. 9(c) and (d).

Here, we consider the relationship between the natural frequencies of the uncoupled system and those of the coupled system. In Fig. 9(a), one can see the coupled (or uncoupled) added mass frequency region with downward sloping in the  $\Omega - \bar{m}$  plane, in regions of smaller  $\bar{m}$  than that of this region, i.e.,  $\bar{m} = 0.01$ . In addition, one can see that the coupled natural frequencies of the first and second modes, indicated by the red and blue curves, respectively, are slightly lower than those of uncoupled beam frequency values, which are indicated by dotted lines. In the region with larger  $\bar{m}$ , i.e.,  $\bar{m} = 100$ , the coupled natural frequencies of the second and third modes, indicated by blue and green lines, respectively, are slightly higher than the uncoupled values. This means that the magnitude relationship of the uncoupled and coupled natural frequencies depends on whether a region with smaller or larger  $\bar{m}$  crosses the added mass frequency region.

### 3.4 Coupled vibration modes

#### 3.4.1 Influence of added mass ratio $\bar{m}$

The coupled natural frequency curves and the corresponding vibration modes are shown in Fig. 10 for  $\bar{M} = 0$ ,  $\kappa = 100$ , and  $\bar{m} = 0.01, 1.0, 10.0, 100.0$ . In this case, for  $\bar{M} = 0$ , the influence of liquid motion on the main body and the beams is significant. In the figures of vibration mode,



(a)

Fig. 10 Coupled vibration modes with  $\bar{m} : \bar{M} = 0$ ,  $\kappa = 100$

deflections of the beams and the added mass are both shown from zero; the added mass position is marked with a green circle, and the amplitudes of the beams and the added mass are normalized such that the maximum of either is unity.

When  $\bar{m} = 0.01$ , as in Fig. 10(b), the beam motion is predominant in the coupled first, second, and fifth modes, whereas the added mass motion is predominant in the third and fourth modes. As  $\bar{m}$  increases to  $\bar{m} = 1$ , as in Fig. 10(c), the added mass motion is predominant in the first and second modes. For further increase to  $\bar{m} = 10, 100$ , as in Figs. 10(d) and (e), for modes higher than the second mode, the added mass motion is nearly zero.

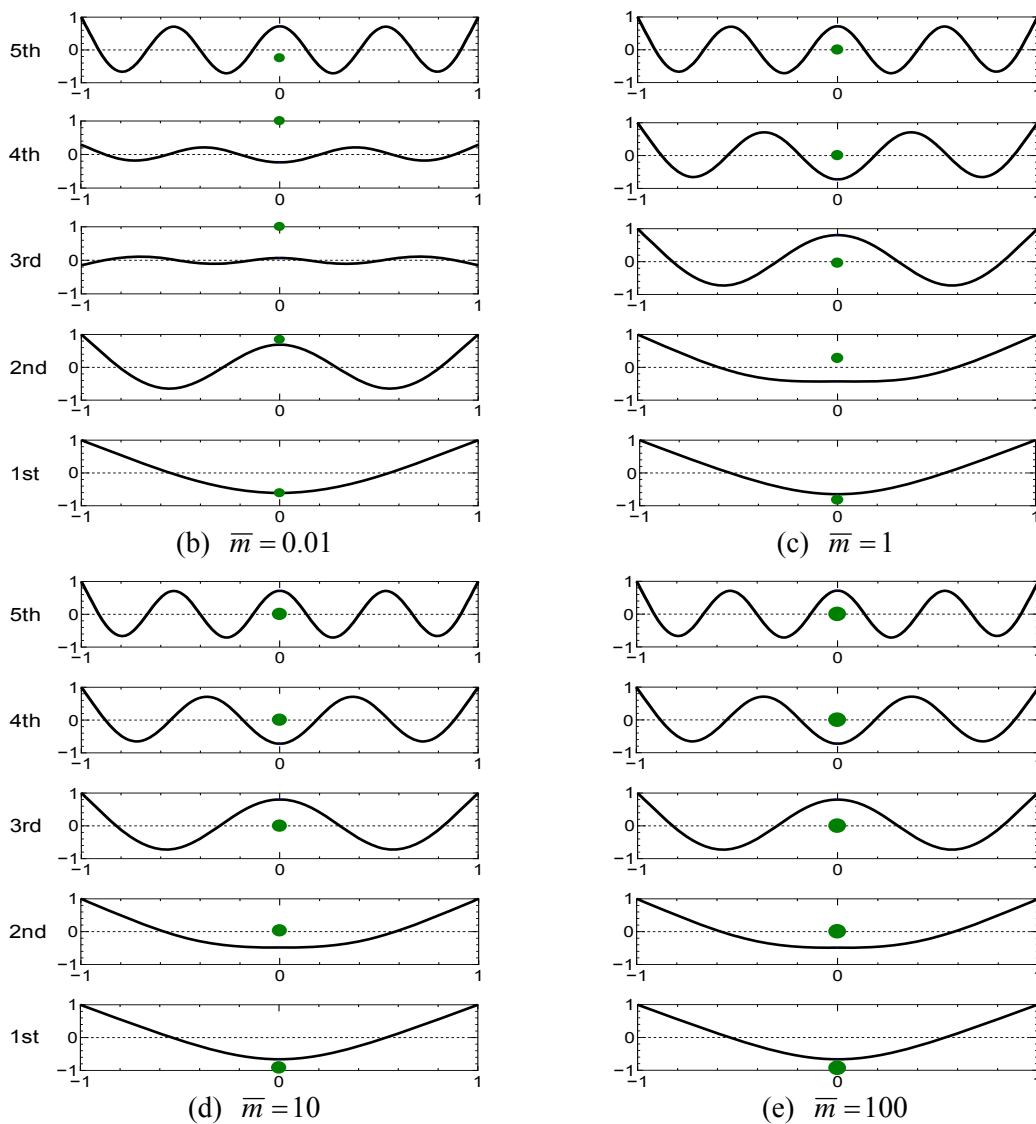


Fig. 10 Coupled vibration modes with  $\bar{m} : \bar{M} = 0$ ,  $\kappa = 100$ ; (b)  $\bar{m} = 0.01$ ; (c)  $\bar{m} = 1$ ; (d)  $\bar{m} = 10$ ; (e)  $\bar{m} = 100$

Comparing the vibration modes and the coupled natural frequency curves, we find that the added mass motion is predominant in the regions where the coupled natural frequencies are close to the uncoupled natural frequency curve of the added mass. In contrast, beam motion is predominant in the region in which the coupled natural frequencies are near the uncoupled natural frequency curve of the beam, except for the first mode, when  $\bar{m} = 10, 100$ , which comes from the assumption  $\bar{M} = 0$ . Variations of the coupled added mass mode can be recognized clearly. That is, with an increase in  $\bar{m}$ , the coupled added mass mode couples with lower beam mode, and the displacement of added mass decreases in the coupled beam modes.

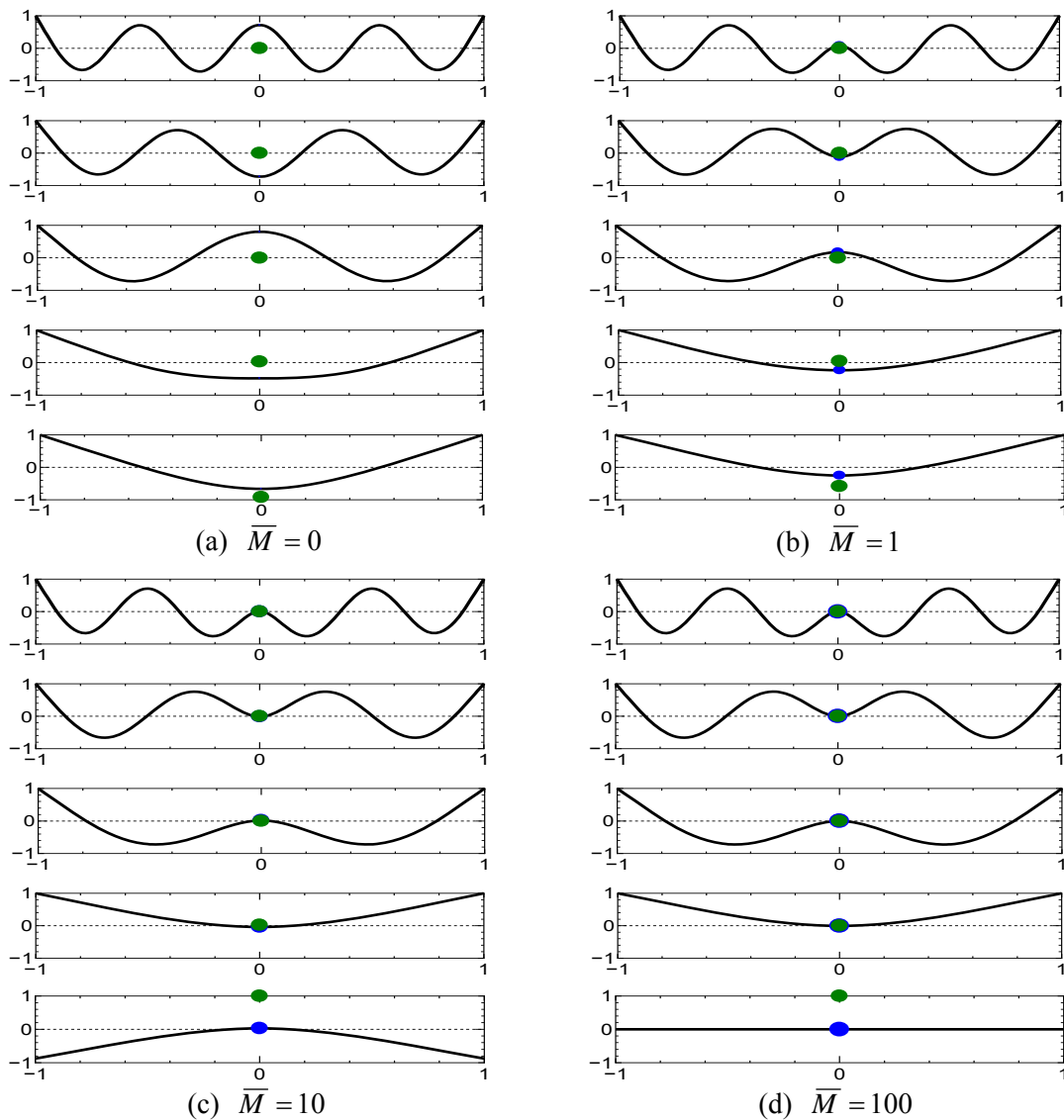


Fig. 11 Coupled vibration modes with  $\bar{M} : \bar{m} = 10, \kappa = 100$ ; (a)  $\bar{M} = 0$ ; (b)  $\bar{M} = 1$ ; (c)  $\bar{M} = 10$ ; (d)  $\bar{M} = 100$

### 3.4.2 Influence of main mass ratio $\bar{M}$

Next, we discuss the influence of  $\bar{M}$ . Variations of the coupled vibration modes with  $\bar{M}$  are shown in Fig. 11 for  $\bar{M} = 0, 1, 10, 100$ ;  $\bar{m} = 10$ ; and  $\kappa = 100$ . In the figure, positions of the added mass and the main body are indicated by green and blue circles, respectively. In Fig. 11(a), because  $\bar{M} = 0$ , the beam center moves in all modes, and the coupled first mode is the coupled added mass mode.

For  $\bar{M} = 1$ , as in Fig. 11(b), the displacement of the beam center decreases to be less than that for  $\bar{M} = 0$ . For  $\bar{M} = 10$ , as in Fig. 11(c), the displacement of the beam center becomes nearly zero, even in the coupled added mass mode. At last, for  $\bar{M} = 100$ , as in Fig. 11(d), in the coupled added mass mode, i.e., the lowest mode, beam vibration disappears.

### 3.5 Coupling strength

Here, we introduce the parameter  $EV$  (Evaluation Value), which quantitatively estimates the coupling strength between the beam and added mass motions and is a product of the absolute value of the displacement of the beam tip  $w(1)$  and the added mass (liquid)  $\zeta$ . A large  $EV$  value represents stronger coupling between the beam and the added mass motion.

$$EV = |w(1)| \times |\zeta|$$

The coupled natural frequency curves of the first and second modes for  $\bar{M} = 10, \kappa = 100$ , and  $\bar{m} = 1 \sim 50$ ; coupling strength  $EV$ ; and variations of the vibration mode with  $\bar{m}$  are shown Fig. 12. In Fig. 12(a),  $EV$  values are indicated on the curves by circles, the diameters of which are proportional to the respective  $EV$  values.

At first, looking at the  $EV$  curve for the first mode, indicated in Fig. 12(b) by the red curve, as  $\bar{m}$  increases from  $\bar{m} = 1$ , the curve reaches its maximum value close to  $\bar{m} = 8$ , and decreases with any further increase in  $\bar{m}$ . One can see from the vibration modes shown in the left-hand side of the figure that at its peak near  $\bar{m} = 8$ , both the displacement of the added mass and that of the beam tip reach their respective maximum values. However, in the  $EV$  curve of the second mode, indicated in blue, reaches its maximum value at  $\bar{m} = 2.5$ . Furthermore, contrary to the first mode case, the motions of the added mass and the beam are out of phase, as can be seen in the vibration modes shown in the right-hand side of the figure.

In the coupled frequency curves shown in Fig. 12(a), since the two curves are the most nearest in the neighborhood of  $\bar{m} = 4$ , one usually presumes that the coupling is the largest in this region. It should be noted, however, that the coupling strength increases in the regions corresponding to  $\bar{m} = 2.5, 8.0$ , crossing the region with  $\bar{m} = 4$ , as shown in Figs. 12(a) and (b). Thus, from the variations in the vibration mode, it is clear that in this region, the frequency curves veer. In addition, in the region with larger and smaller values of  $\bar{m} = 4$ , the phases of the added mass motion and the beam motion are inverted, and in the transition region, where the two aforementioned phases are inverted, the amplitude of either the added mass or the beam becomes zero.

Next, at the beginning, when  $\bar{m} = 1$ , the coupled first mode is the first beam mode, whereas the coupled second mode is the added mass mode. As  $\bar{m}$  increases, the natural frequency curves asymptotically close each other and veer instead of crossing; the exchange of vibration modes

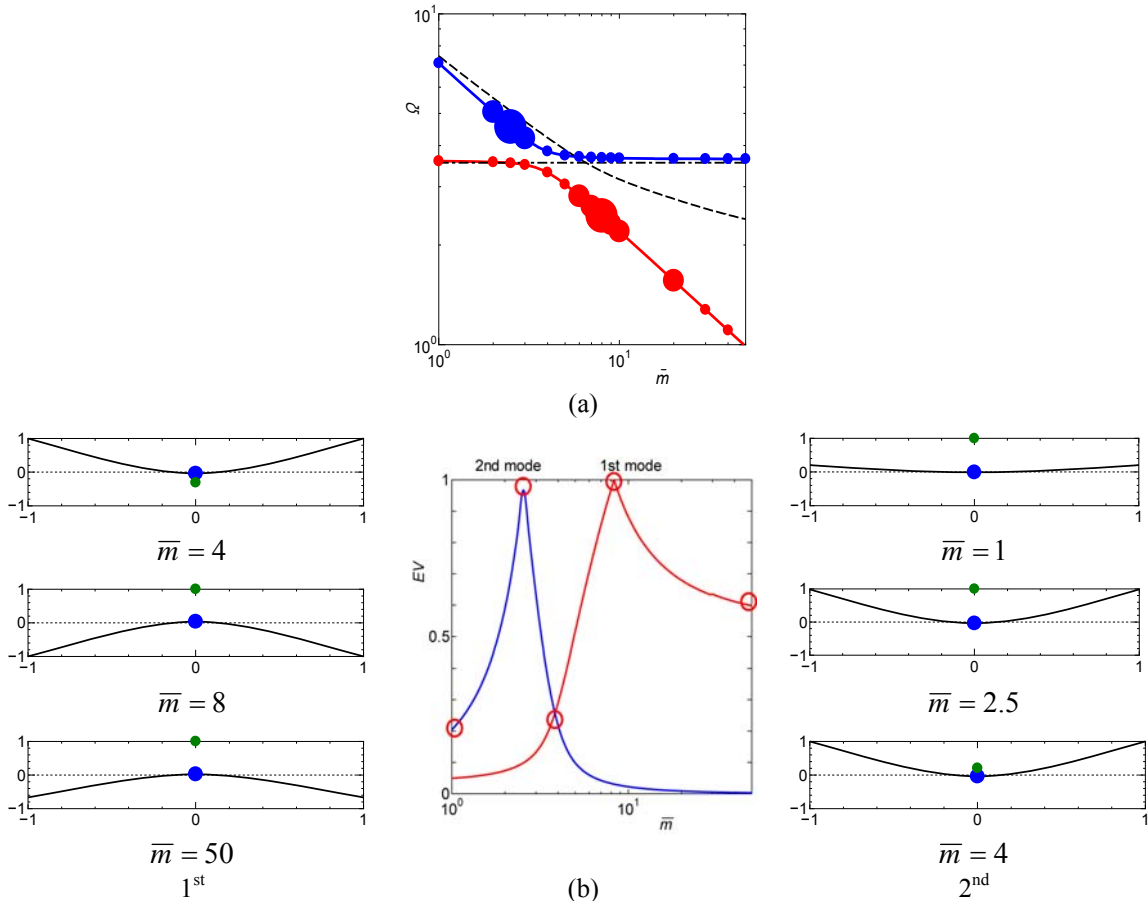


Fig. 12 Variation in evaluation value  $EV$  with  $\bar{m}$ :  $\bar{M} = 10, \kappa = 100$ ; (a) Coupled natural frequency curves; (b)  $EV$  and vibration modes with  $\bar{m}$

occurs, i.e., the coupled first mode tends toward the added mass mode, and the coupled second mode tends toward the beam mode.

In actual satellites, as operations proceed, i.e., as time passes,  $\bar{m}$  decreases gradually, whereas the fuel sloshing frequency increases gradually and approaches that of the flexible appendages. This generates the possibility of strong coupled motion in two regions of  $\bar{m}$  instead of one.

#### 4. Conclusions

The coupled free vibration analysis of flexible structures and on-board liquid in zero-gravity space was conducted. The spacecraft main body was modeled as a rigid mass, flexible appendages as two elastic beams, and on-board liquid as a “spring-mass” system. Currently, coupled dynamic systems are represented by three system parameters, i.e., mass ratio  $\bar{M}$ , added mass ratio  $\bar{m}$ , and spring rigidity parameter  $\kappa$ .

The obtained results are summarized as follows:

**Types of coupled natural vibration**

- There are two types of vibration in the coupled system: one in which the beam (appendages) motion is predominant and the other in which the added mass (liquid) motion is predominant.
- As  $\bar{m}$  increases, the frequency of the former type of vibration remains nearly constant, whereas that of the latter type of vibration, i.e., coupled added mass, decreases.
- As  $\kappa$  increases, the coupled added mass frequency increases over the parameter range of  $\bar{m}$ , which leads to an increase in the number of the coupling regions with the beam modes as well as in the value of  $\bar{m}$ .

**Influence of added mass**

- In actual spacecraft, as fuel is consumed step by step, i.e.,  $\bar{m}$  decreases gradually, at some fuel mass  $\bar{m}$ , the sloshing frequency approaches that of the beam (flexural appendages), and a strong coupled motion is expected to occur. For lower  $\bar{m}$  values, coupling occurs with higher-order structural modes.

**Influence of main body mass**

- When the mass of the main body is small, the influence of liquid sloshing on the main body is significant. Therefore, vibrations can be generated in the elastic appendages that are fixed to the main body, and the region in which the liquid motion and appendage motion couple widens. In this case, even when the fuel tank is empty, the influence of beam motion on the main body is significant.
- When the mass of the main body is large, the influence of liquid sloshing motion on the main body is small. Then, it is difficult to generate vibrations in the appendages, and the coupled region is narrow. In this case, the influence of beam motion on the main body is small, and it is difficult to generate vibration in the liquid.

**Mode exchanges and coupling strength**

- When a system parameter, i.e.,  $\bar{m}$ , varies, two coupled natural frequency curves asymptotically close each other and veer instead of crossing. At that time, vibration modes are exchanged, which reverses the phases of the directions of liquid motion and beam motion. The strength of the coupling is large not at closest region of the two frequency curves, but at two regions separate from this region.

**References**

Abramson, H.N. (1966), *The dynamic behavior of liquids in moving containers*, Chapter 11, NASA SP-106.  
 Agrawal, B.N. (1993), "Dynamic characteristics of liquid motion in partially filled tanks of a spinning spacecraft", *J. Guid. Control. Dynam.*, **16**(4), 636-640.  
 Bauer, H.F. and Eidel, W. (1990a), "Linear liquid oscillations in cylindrical container under zero gravity", *Appl. Microgravity Tech.*, **II**, 212-220.  
 Bauer, H.F. and Eidel, W. (1990b), "Small amplitude liquid oscillations in a rectangular container under zero gravity", *Zeitschrift für Flugwissenschaften und Weltraumforschung*, **14**(1-2), 1-8.

- Berglund, M.D., Bassett, C.E., Kelso, J.M., Mishic, J. and Schrange, D. (2007), "The Boeing Delta IV launch vehicle—Pulse-settling approach for second-stage hydrogen propellant management", *Acta Astronaut.*, **61**, 416-424.
- Buzhinskii, V.A. (2009), "The equations of the perturbed motion of a rocket as a thin-walled structure with a liquid", *J. Appl. Math. Mech.*, **73**, 692-695.
- Chiba, M., Watanabe, H. and Bauer, H.F. (2002), "Hydroelastic coupled vibrations in a cylindrical container with a membrane bottom, containing liquid with surface tension", *J. Sound. Vib.*, **251**(4), 717-740.
- Farhat, C., Chiu, E.K. and Amsallem, D. (2013), "Modeling of fuel sloshing and its physical effects on flutter", *AIAA J.*, **51**(9), 2252-2265.
- He, Y.J., Ma, X.R., Wang, P.P. and Wang, B.L. (2007), "Low-gravity liquid nonlinear sloshing analysis in a tank under pitching excitation", *J. Sound. Vib.*, **299**, 164-177.
- Komatsu, K. (1999), "Modeling of the dynamic behavior of liquids in spacecraft", *Int. J. Microgravity Sci. Appl.*, **16**(3), 182-190.
- Komatsu, K. and Shimizu, J. (1989), *Dynamic behavior of liquid in spacecraft (in Japanese)*, NAL-NASDA Report.
- Lü, J., Li, J.F. and Wang, T.S. (2005), "Dynamic response of liquid filled rectangular tank with elastic appendages under pitching excitation", *Appl. Math. Mech-Engl.*, **28**(3), 351-359.
- McIntyre, J.E. and McIntyre, J.M. (1982), "Some effects of propellant motion on the performance of spinning satellites", *Acta Astronaut.*, **9**(11), 645-661.
- Santini, P. and Barboni, R. (1978), "Motion of orbiting spacecrafts with a sloshing fluid", *Acta Astronaut.*, **5**(7-8), 467-490.
- Santini, P. and Barboni, R. (1983), "A minicomputer finite elements program for microgravity hydroelastic analysis", *Acta Astronat.*, **10**(2), 81-90.
- Utsumi, M. (2004), "A mechanical model for low-gravity sloshing in an axisymmetric tank", *Trans. ASME, J. Appl. Mech.*, **71**, 724-730.
- Vreeburg, J.P.B. (2008), "Sloshsat spacecraft calibration at stationary spin rates", *J. Spacecraft. Rockets*, **45**(1), 65-75.

**Appendix A. Parameter  $\alpha_m$**

Parameter  $\alpha_m$  ( $m = 1 \sim 10$ ) that satisfies the frequency eq. (14) is presented in Table A1. When  $\bar{M} = 0$ ,  $\alpha_m$  tends to the eigenvalue of a free-free beam of length  $2l$ , whereas when  $\bar{M} \rightarrow \infty$ ,  $\alpha_m$  tends to the eigenvalue of a cantilever beam of length  $l$ .

Table A1  $\alpha_m$  as a function of  $\bar{M}$

$\bar{M} = 0$	0.5	1	2	3	4	5	10	$\bar{M} = \infty$
2.3650	2.1362	2.0540	1.9851	1.9546	1.9374	1.9263	1.9022	1.8751
5.4978	4.9820	4.8686	4.7916	4.7618	4.7459	4.7361	4.7156	4.6941
8.6394	8.0509	7.9657	7.9140	7.8952	7.8854	7.8795	7.8673	7.8548
11.7810	11.1465	11.0782	11.0388	11.0249	11.0177	11.0134	11.0045	10.9955
14.9226	14.2596	14.2029	14.1712	14.1602	14.1545	14.1511	14.1442	14.1372
18.0642	17.3816	17.3330	17.3068	17.2977	17.2930	17.2902	17.2845	17.2288
21.2058	20.5090	20.4669	20.4442	20.4364	20.4324	20.4300	20.4252	20.4204
24.3473	23.6398	23.6026	23.5827	23.5759	23.5724	23.5704	23.5662	23.5619
27.4889	26.7729	26.7396	26.7219	26.7159	26.7128	26.7110	26.7073	26.7035
30.6305	29.9077	29.8775	29.8616	29.8562	29.8534	29.8518	29.8485	29.8451

**Appendix B. System parameter ranges**

Typically, in liquid-fuel rockets, the liquid propellant and liquid oxidant constitute about 60% to 90% of the rocket’s launch mass, see Komatsu and Shimizu(1989); this figure is about 10% for satellites. For a satellite equipped a liquid apogee motor, the liquid fuel constitutes about half of its mass. Then, liquid mass  $m_F$  is assumed to be 10%–50% of the dry mass  $m_D$  of satellites.

Here, because launch mass  $m_L$  is the sum of  $m_F$  and  $m_D$ , i.e.,  $m_L = m_D + m_F$ , the ratio of liquid mass to launch mass,  $\sigma_F (= m_F / m_L)$ , is

$$\sigma_F = \frac{m_F}{m_L} = \frac{m_F}{m_D + m_F} = \frac{0.1 \sim 0.5}{1 + (0.1 \sim 0.5)} = 0.07 \sim 0.45 \tag{A1}$$

As the dry mass includes the mass of the solar paddles, we estimate the mass of the solar paddles. Under the assumption that power generated per unit mass of solar paddle is 20–100 W, the presumed paddle mass to the launch mass ratios are summarized in Table A2. From the table, the ratio of the paddle mass to the launch mass is estimated as follows

$$\sigma_p (= m_p / m_L) = 0.006 \sim 0.13 \tag{A2}$$

Using parameters employed in the present analysis, i.e., mass of main body  $M$ , mass of solar paddles  $2\rho Al$ , mass of liquid  $m$ ,  $m_L$  is expressed as follows

$$m_L = m_D + m_F = M + 2\rho Al + m$$

Table A2 Presumed paddle mass ratio [2]

Satellite	Mass [kg]	Power [W]	Presumed paddle mass [kg]	Paddle mass ratio [%]
ETS-VIII	2800	7500	75 ~ 375	2.68 ~ 13.4
DRTS	2800	2100	21 ~ 105	0.75 ~ 3.75
TRMM	3620	3300	33 ~ 165	0.91 ~ 4.56
EOS-PM1	3100	4860	48.6 ~ 243	1.57 ~ 7.84
ALOS	4000	7000	70 ~ 350	1.75 ~ 8.75
GOSAT	1650	3300	33 ~ 165	2 ~ 10
WINDS	2700	5200	52 ~ 260	1.93 ~ 9.63
OICETS	570	1220	12.2 ~ 61	2.14 ~ 10.7
SWAS	102	59	0.59 ~ 2.95	0.58 ~ 2.89

and using the liquid mass ratio  $\sigma_F$  and the paddle mass ratio  $\sigma_P$ ,

$$m_L = M + \sigma_P m_L + \sigma_F m_L$$

From above two equations, one obtains the following

$$M = (1 - \sigma_F - \sigma_P) m_L \quad (\text{A3})$$

$$m = m_L - M - 2\rho A l = m_L \sigma_F \quad (\text{A4})$$

Normalizing with the paddle mass, one obtains the following parameter ranges

$$\bar{M} = \frac{M}{\sigma_P m_L} = \frac{1 - \sigma_F - \sigma_P}{\sigma_P} = 3.20 \sim 154$$

$$\bar{m} = \frac{m}{\sigma_P m_L} = \frac{\sigma_F}{\sigma_P} = 0.54 \sim 90.0$$

Then, we use the main mass ratio  $\bar{M}$  as 1–200 and the added mass ratio  $\bar{m}$  as 0.5–100 for the numerical calculations.

### Appendix C. Non-dimensional natural frequency $\Omega_{2FF}$ of free–free beam with non-dimensional length 2

Frequency equation of a free-free beam with length  $l$  is as follows

$$\cos \alpha_n \cosh \alpha_n - 1 = 0, \quad \left( \alpha_n^2 = \omega_{FF}^2 l^2 \sqrt{\frac{\rho A}{EI}} = \frac{\omega_{FF}}{\omega_b} \right) \quad (\text{A5})$$

where  $\alpha_n$  is a parameter listed in Table A3. From Eq. (A5), the natural circular frequency is as follows

$$\omega_{FF} = \frac{\alpha_n^2}{l^2} \sqrt{\frac{EI}{\rho A}} \tag{A6}$$

Substituting the length as  $l \rightarrow 2l$ , one obtains the following

$$\omega_{2FF} = \left(\frac{\alpha_n}{2}\right)^2 \frac{1}{l^2} \sqrt{\frac{EI}{\rho A}} \tag{A7}$$

In the non-dimensional form

$$\Omega_{2FF} = \frac{\omega_{2FF}}{\omega_b} = \left(\frac{\alpha_n}{2}\right)^2 \tag{A8}$$

The non-dimensional natural circular frequency  $\Omega_{2FF}$  of a free-free beam with a non-dimensional length of 2 is found to be a square of  $\alpha_n/2$  and is listed in Table A3.

Table A3. Eigenvalues and non-dimensional natural frequencies  $\Omega_{2FF}$ : free-free beam (non-dimensional length is 2)

	1 <sup>st</sup>	2 <sup>nd</sup>	3 <sup>rd</sup>	4 <sup>th</sup>	5 <sup>th</sup>	6 <sup>th</sup>	7 <sup>th</sup>	8 <sup>th</sup>	9 <sup>th</sup>
$\alpha_n$	4.73	7.85	11.0	14.1	17.3	20.4	23.6	26.7	29.8
$\alpha_n/2$	2.37	3.93	5.50	7.07	8.64	10.2	11.8	13.4	14.9
$\Omega_{2FF} = (\alpha_n/2)^2$	5.59	15.4	30.2	50.0	74.6	104	139	178	223